Nanoscale

ROYAL SOCIETY OF CHEMISTRY

PAPER

View Article Online
View Journal | View Issue

Cite this: *Nanoscale*, 2024, **16**, 19453

Design of "green" plasmonic nanocomposites with multi-band blue emission for ultrafast laser hyperthermia†

Yury V. Ryabchikov

Although non-toxic nanoscale materials are widely employed for different healthcare applications, their performance is still considerably limited. In this paper, various approaches using the environmentally friendly ultrafast laser processing were employed to remodel IV group semiconductor nanostructures and synthesize highly-stable (ξ-potential is up to −47 mV) colloidal solutions of plasmonic (525 nm) nanocomposites with a strong size-dependent chemical content. All nanocomposites exhibited a remarkable lamp-excited multi-band blue emission centred at around 420 nm that is considerably (~10-fold for Au–SiC) stronger than from nanocomposites prepared by the laser co-fragmentation technique. The latter formed a greater quantity of smaller narrowly dispersed (~4 nm for Au–Si) plasmonic nanostructures compared to the direct laser ablation method. Moreover, it led to a greater number of semiconductor elements (~1.7-fold for Au–Ge) in the nanocomposites, which was correlated with lower (~30%) electrical conductivity. Aqueous colloidal solutions revealed a greater degree (~80%) of the femtosecond laser-induced heating for all nanocomposites formed by direct laser ablation. These findings highlight the peculiarities of the applied laser processing approaches and considerably facilitate the design of specific multi-modal plasmonic-fluorescence (biosensing, bioimaging, hyperthermia) nanocomposites with a required performance that significantly expands the application area of semiconductor nanostructures.

Received 29th July 2024,
Accepted 16th September 2024

DOI: 10.1039/d4nr03120b

rsc.li/nanoscale

Introduction

The continuous fast development of nanotechnologies has led to the production of novel low-dimensional materials, revealing new unique features that can be used in different life science applications. Here, silicon-based nanostructures are one of the most promising and most studied materials and are widely employed in healthcare applications due to their excellent bio-safety.[1–3] They were successfully demonstrated as efficient singlet oxygen photosensitizers,[4–6] as well as anti-cancer drug delivery platforms for the therapy of oncological[7,8] and cardiovascular diseases.[9–11] Moreover, silicon-containing nanostructures are efficient contrast agents in optical bio-imaging[12–14] and optical coherence tomography (OCT).[15,16] They also can efficiently catalyse hydrogen generation,[17,18] or they can be used as nanoscale thermometers.[19,20] Complex silicon-based nanohybrids have revealed efficient anti-microbial actions with further applications in dentistry as fillers, or in food storage as an alternative to plastic packaging materials.[21–23] Considerable prospective applications for anti-microbial purposes, for treating Alzheimer's disease, or near-infrared-II photoacoustic imaging were also demonstrated using germanium (Ge) nanoparticles (NPs).[24–26] Another promising element of the IV group is carbon (C), whose low-dimensional structures are also very important for various biomedical applications.[27–29] However, in most cases, their application range is considerably restricted by their specific properties, requiring the employment of several nano-agents.

Ultrafast laser processing is a very efficient method for treating both bulk and nanostructured materials to control their functional properties. Its advantages include the high precision of the laser treatment localisation and ultrapure chemical conditions, which are very favourable for biomedical applications of the laser-functionalized (nano-)materials. This allows significant modification of the target surface, leading to new specific features as compared to the initial materials.[30–33] It can also precisely change the volume of materials, which can be promising for different practical applications, *e.g.*, for photocatalytic activity or the development of colour displays.[34–37] Moreover, it was recently shown that ultrafast laser processing is a simple and efficient route to expand the performance of semiconductor NPs.[38–40] Their functional properties are considerably improved by merging semiconductor

HiLASE Centre, FZU – Institute of Physics of the Czech Academy of Sciences, Za Radnicí 828, 25241 Dolní Břežany, Czech Republic. E-mail: ryabchikov@fzu.cz

† Electronic supplementary information (ESI) available. See DOI: https://doi.org/10.1039/d4nr03120b

nanostructures with metallic elements, which is caused by the impact of ultrafast laser pulses, leading to promising applications of laser-generated nanocomposites (NCs).[41–43] However, the use of ultrafast laser processing in the development and application of semiconductor-metallic NCs with controllable specific features is still very challenging because of the very limited number of publications in this regard. Thus, it is necessary to examine the laser-assisted interaction between different semiconductor and metallic nanostructures with required performance in a liquid environment to design compound nanostructures for multi-modal healthcare applications.

In this paper, we report the formation of NCs revealing a strong plasmonic absorption maximum (525 nm) based on different IV group semiconductors (such as silicon, silicon carbide and germanium) by using two different ultrafast laser processing approaches: direct laser ablation (LA) and laser co-fragmentation (LcF). We found a larger nanoparticle concentration (~10^{12} NPs per mL) with a lower size distribution for composite nanostructures formed by the LcF approach in comparison with the direct LA one that also exhibited a strong multi-band blue (~420 nm) emission. All colloidal solutions showed excellent chemical stability with ξ-potential values around −35 mV, which is ~20–25% higher for co-fragmented NPs. Moreover, the latter demonstrated ~30% lower electrical conductivity than the nanostructures formed by the direct LA approach. All NCs revealed strong size-dependent chemical composition for nanoparticles smaller than 30 nm. At the same time, plasmonic NCs synthesized by the LcF approach showed a greater content of semiconductor elements in comparison with nanostructures prepared by the direct LA. Our findings demonstrate the facile expansion of functional properties of the IV group semiconductor nanostructures that can be finely controlled by conditions of the laser-matter interaction.

Materials and methods

To synthesize plasmonic nanocomposites based on various IV group semiconductors, the following multi-step ultrafast laser processing techniques were employed. Firstly, pure metallic (Au) and semiconductor (Si, SiC, Ge) nanoparticles were prepared by direct pulsed laser ablation in liquids (PLALs) of a corresponding target that were also used as references. Secondly, composite NPs were formed using either direct laser ablation or laser co-fragmentation approaches (Fig. 1). In the first case, the gold target was ablated in the previously prepared colloidal solutions of semiconductor NPs (Si NPs, SiC NPs, Ge NPs) taken in an equal mass concentration (0.1 g L^{-1}). In the second case, a mixture of colloidal solutions of metallic and semiconductor NPs (1 : 1 volume ratio) were irradiated using the same laser irradiation conditions. To homogenize colloidal solutions, they were continuously stirred prior and during laser irradiation. To retain the same semiconductor NPs concentration in a volume unit for both approaches, the colloidal solutions were diluted by 2-fold with deionized water prior to the laser ablation of the gold target (LA approach) (Fig. 1).

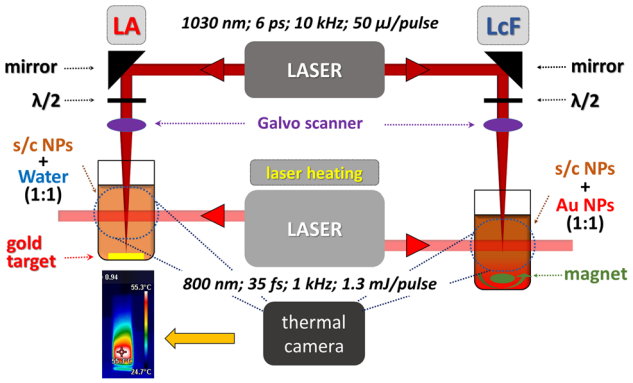

Fig. 1 A sketch of ultrafast laser processing experiments for the synthesis and heating of semiconductor-plasmonic nanocomposites.

Laser synthesis of both single- and multi-element NPs was performed in a glass vessel by means of a pulsed laser (6 ps pulse duration, 10 kHz repetition rate) at 1030 nm wavelength and 50 μJ per pulse laser fluence. In the case of the LA approach, the laser irradiation was focused into a 50 μm spot size on the surface of the used solid state targets. Meanwhile, in the case of the LcF approach, the focal plane was located 4 mm below the air/liquid interface (Fig. 1). The laser processing time was 180 s.

With the aim of visualising the composite plasmonic NPs, a high-resolution transmission electron microscope (HR-TEM) Jeol JEM 3010 operating at 300 kV accelerating voltage was used. A small drop (10 μL) of freshly prepared aqueous solution was placed on a carbon-coated copper grid, and then dried under ambient condition. The calculation of the composite NPs size distributions was performed by means of Image J software using a total of 1000 particles for each sample. To define the chemical composition of various NCs of different sizes, a Jeol JEM 2011 microscope operating at 200 kV accelerating voltage was employed. For this purpose, a single NC isolated from other NPs was selected to avoid any influences from NPs of different sizes, and analysed using energy-dispersive X-ray (EDX) spectroscopy. The corresponding ratios between different chemical elements for NPs of different sizes were identified using a microscope software.

The chemical stability (ξ-potential) and electrical conductivity of colloidal solutions of NPs were investigated using the Malvern Zetasizer Ultra device. Additionally, the nanoparticle conductivity was studied by Hanna PWT HI 98308 operating in the range of 0–99.9 μS cm^{-1} with 0.1 μS cm^{-1} sensitivity. To study the particle concentrations and their hydrodynamic sizes, the colloidal solutions were diluted by 20-fold to avoid an influence of concentration effects on the aforementioned parameters. Hydrodynamic sizes of NCs were studied using the multi-angle dynamic light scattering (MA-DLS) approach at 13°, 90° and 173°. Absorbance spectra of all NP colloidal solu-

tions (2 mL) were investigated by means of a Shimadzu-2600 apparatus equipped with an integrating sphere using the absorption mode, 2 nm slit, 2 s acquisition time, and medium scanning speed.

Photoluminescence (PL) measurements were carried out using a commercial Edinburgh FLS1000 spectrometer equipped with an ozone-free Xenon arc lamp (450 W), both excitation and emission double monochromators with 350 mm focal distances and straight light suppression better than 10^{-10}, as well as a Hamamatsu PMT928P photomultiplier tube (PMT) for signal detection. The PL of plasmonic NCs (1 mL of aqueous solutions in quartz cuvettes) was excited at ~300–310 nm wavelength (corresponding to the maximum excitation efficiency), and detected in the 320–750 nm spectral range with 2 nm step, 1 s acquisition time and 5 scans. The luminescence mapping of the NCs was excited in the 250–400 nm range, and detected in the 350–600 nm range with 2 nm steps, 2 nm excitation and emission bandwidths, and 1 s acquisition time. The UV-Vis and PL measurements were performed using the initial concentrations of the colloidal solutions.

Ultrafast laser heating of the colloidal solutions (1 mL) of plasmonic IV group semiconductor NCs was performed using pulsed (35 fs) laser irradiation at 800 nm with 1000 Hz repetition rate at 1.3 W average power. The images were obtained by a Bosch GTC400C thermal camera during 600 s of the laser irradiation (Fig. 1).

Results and discussion

To visualize the plasmonic NCs formed using various IV group semiconductors, the NCs dried on carbon-coated grid composite NPs were investigated by HR-TEM (Fig. 2). It was found that different NCs (Au–Si, Au-SiC, Au–Ge) demonstrated similar microscopic images of spherically-shaped NPs with mean sizes of around 8–10 nm. Nevertheless, the TEM observation of Au–Ge NPs also highlighted their worse size dispersion homogeneity in comparison with the Si-based nanostructures due to the presence of larger NPs (Fig. 2). Moreover, all plasmonic NCs prepared *via* different laser processing approaches (LA or LcF) possessed a multi-crystalline structure due to the presence of several gold crystalline planes, similar to the previously published findings.[39] The estimated size distributions of various composite NPs revealed the following peculiarities.

Firstly, all plasmonic NCs demonstrated considerably smaller mean sizes (Fig. 3) as compared to pure NPs (both

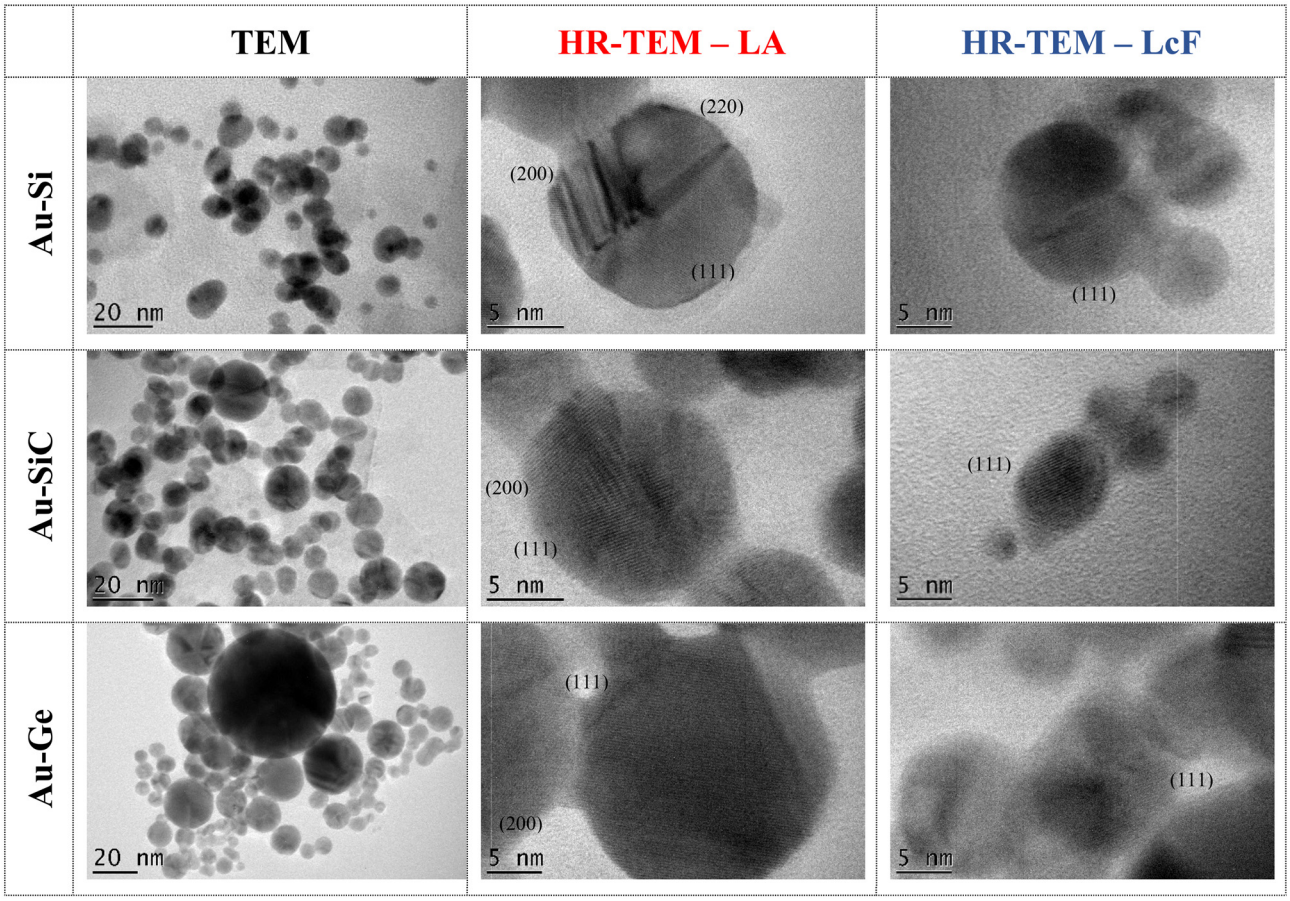

Fig. 2 TEM images of metallic-semiconductor NCs formed by ultrafast laser processing.

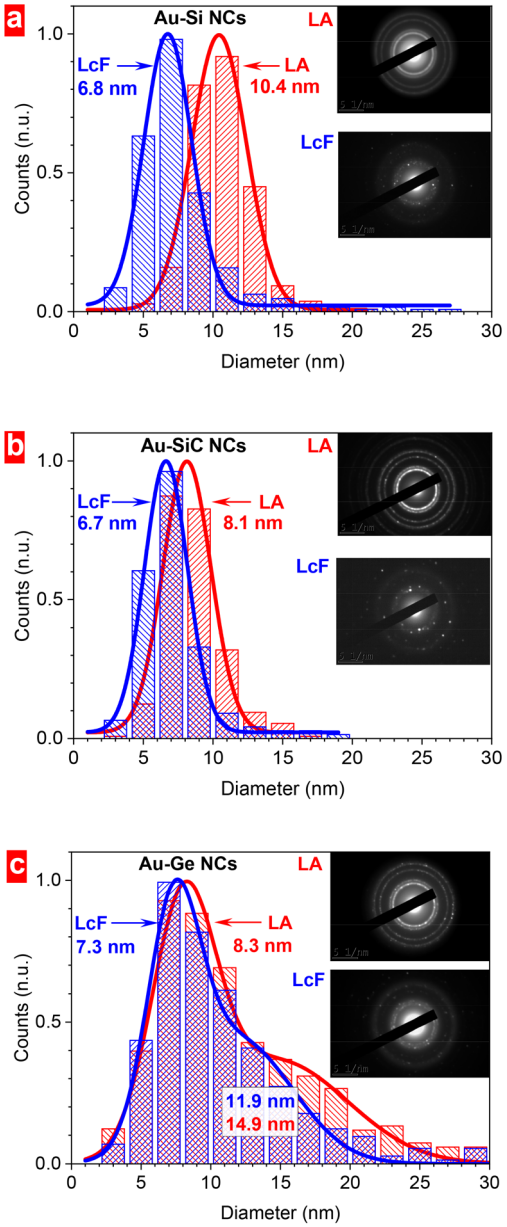

Fig. 3 Size distributions and corresponding diffraction patterns of metallic-semiconductor NCs: (a) Au–Si, (b) Au-SiC, (c) Au–Ge.

metallic or semiconductor) formed in deionized water (~30–40 nm) without any additives.[39,44] Indeed, it is known that the environment above the ablated targets plays a significant role in the dynamics of the laser plume.[45] Hence, the presence of semiconductor NPs in a liquid will considerably affect the composition of the laser-generated plume and its dynamics, changing the mechanisms of the nanoparticle growth as compared to single-element ones. In the case of PLALs, one can divide the whole process into the following stages:[46]

– *Early stage*: the absorption of the deposited laser energy, the ejection of nanostructures of the involved materials, and the formation of the laser plume;

– *Intermediate stage*: the expansion of the laser plume in the presence of a confining liquid medium;

– *Late stage*: mixing of the laser plume with the liquid and nanoclusters, followed by further coalescence/aggregation processes.

Thus, the presence of semiconductor NPs in water during laser ablation can influence the processes that occur in all of the aforementioned stages, being affected by their size, concentration or chemical composition. Firstly, the composition of the laser-induced plasma plume will change due to the fragmentation of semiconductor NPs affected by the laser irradiation. Evidently, the chemical content of the plasma plume will depend on the concentration of NPs, their velocity in a liquid, applied laser energy, *etc*. Secondly, semiconductor nanoclusters will attenuate the laser energy, leading to additional energy losses and causing a shielding effect. Thirdly, they can make an impact on the expansion of the laser-generated plasma plume due to (i) the additional nanostructures beyond it, from one side, and (ii) the changed composition of the plasma plume, from another side. Finally, the semiconductor nanoclusters in the plasma plume can also considerably affect the temperature and pressure distribution, shortening the interaction between nanoclusters, and thus decreasing their size (Fig. 3).

Differences in the size of NPs formed by the LA and LcF approaches can appear due to the significantly different conditions during the creation, expansion, and collapse of the plasma plume. Indeed, during the LcF approach, the plume is formed because of the fragmentation of both Si and Au NPs, while a solid target is a major source of the plume content during the direct LA approach. Thus, LcF can lead to a large number of smaller plasma plumes, which can intermix with each other (Fig. 4b). Their smaller size can restrict the growth of NPs during LcF, which was experimentally observed for all NCs (Fig. 3). The aforementioned differences of the plasma plume properties may also result in different diffraction pattern images (Fig. 3, insets). More pronounced diffraction rings corresponding to the (111), (200), (220), (311) and (222) gold crystalline planes can appear because of the solid target gold nanoclusters, whose interaction can lead to the formation of gold crystalline structures. However, in the case of the LcF approach, the concentration distribution of different elements will be more homogeneous, leading to an amorphous NC structure due to the strong interaction between Si and Au atoms. Moreover, it can also decrease the size of the semiconductor nanodomains.

Secondly, plasmonic silicon-based NCs (Au–Si, Au-SiC) revealed monodisperse narrow size distributions of NPs (Fig. 3) similar to the previously reported data:[40,43] 10.4 nm and 8.1 nm for LA Au–Si and Au-SiC NCs, respectively. However, both types of plasmonic Ge-based NCs possessed bimodal size distributions (8.3 nm and 14.9 nm), as observed for pure Au NPs.[39,47] This can point to various mechanisms of the NP growth during the laser-assisted photo-chemical processes.[39,47] In particular, an impact from the high-power laser irradiation can provoke fast germanium oxidation and

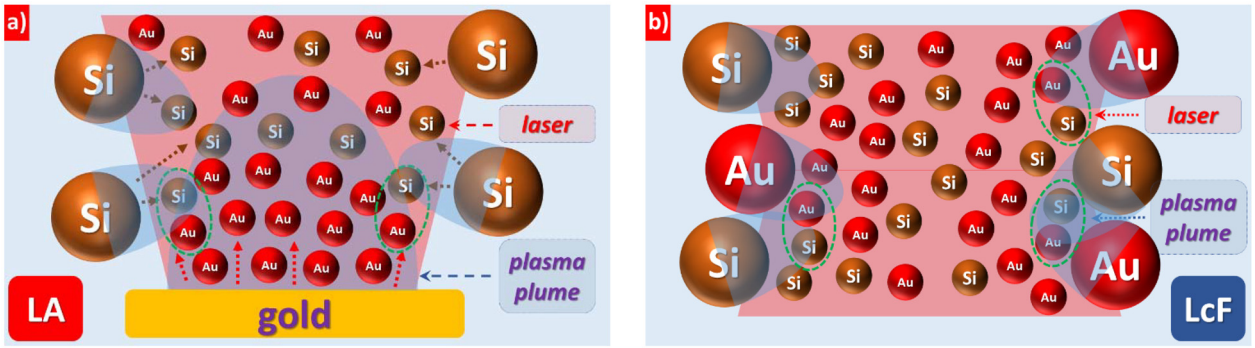

Fig. 4 A sketch of the formation of silicon-gold NCs in deionized water in the case of the: (a) direct LA approach and (b) LcF approach (sizes and shapes of all items differ from real ones).

dissolution in the oxygen-saturated aqueous medium, which is favorable for the growth of Au-based NPs. Thus, to clarify the influence of the semiconductor nanostructures in aqueous solution on the photochemical processes, it is necessary to perform additional studies of the plasma plume dynamics, depending on (i) the properties of the used NPs, and (ii) the applied laser processing approach, supported with molecular dynamics simulations.

Thirdly, all plasmonic NCs formed by the LcF approach showed smaller mean sizes (~35% for Au–Si NCs), as compared to that synthesized by the direct LA approach (Fig. 3). In these cases, we can hypothesize on the different properties and dynamics of the laser-induced plasma plume due to the various shapes and sizes of the ablated targets. Indeed, the direct LA of an extended plane surface (10 mm) can create one relatively large laser-induced plume containing nanoclusters from ablated gold and fragmented semiconductor materials (Fig. 4). These nanoclusters will interact each other during the plume "lifetime". However, the LcF approach can produce many laser-induced plumes that are much smaller in front of the Au and/or semiconductor NPs (Fig. 4). Their sizes and shapes will be permanently changed due to the continuous mixing of the colloidal solutions during LcF. Moreover, plasma plumes containing different elements will also mix with each other, leading to the interaction between metallic and semiconductor nanoclusters. Because of the smaller sizes and more rapid changes of the plumes, the interaction between different clusters can be faster, leading to smaller mean sizes of the formed NCs (Fig. 3).

To confirm the presence of both semiconductor and metallic elements in all NCs, their EDX spectra were investigated using TEM by selecting a single isolated NP that allowed us to study the size-dependent chemical content of the laser-generated NCs (Fig. S1†). The EDX spectra of Au–Si NCs, Au-SiC NCs and Au–Ge NCs revealed several maxima at different energy positions (Fig. 5a–c). All EDX spectra revealed strong copper signals at 0.93 keV (L_α), 8.04 keV (K_α) and 8.91 keV (K_β), evidently coming from the used copper-based TEM grids. Furthermore, a strong signal at 0.26 keV (cut in the spectra) corresponded to the carbon coating of the TEM grids (K_α-line of carbon). Clear signals from gold located at 2.12 keV (M_α) and 9.71 keV (L_α) were also observed for all NCs. Moreover, the Au-SiC and Au–Ge NCs exhibited a remarkable signal at 11.5 keV related to the L_β transition, while in the case of Au–Si NCs, it was not very well pronounced (Fig. 5a–c). These results confirmed the presence of the plasmonic metal in all studied samples.

The EDX spectra also confirmed the presence of the semiconductor elements used in the NCs. Indeed, one can clearly identify silicon in the Au–Si NCs and Au-SiC NCs due to the apparent signal at 1.74 keV (K_α) (Fig. 5a and b). However, no carbon traces were detected in the Au-SiC samples with the TEM grids covered with a carbon film. The peaks at 1.19 and 0.87 keV corresponded to the L_α and K_α transitions in germanium, respectively (Fig. 5c). Thus, the EDX spectra of the plasmonic NCs clearly demonstrated the presence of both metallic and semiconductor elements in a single nanoparticle, whose aspect ratio changed with the size of the studied NPs. The relative ratio between these elements can give us an idea about the mass contribution of the corresponding elements in a NC of a given size (Fig. S2†) that can be further converted into atomic content (Fig. 5d–f).

The size-dependent chemical composition of all plasmonic semiconductor-based NCs highlighted the strong dependences of both mass contribution (Fig. S2†) and element content (Fig. 5d–f) on the size of NPs, especially for that smaller than 20 nm. Here, larger NPs formed by the direct LA approach (>25–30 nm) consisted mainly of gold atoms (~85–90%), with the remaining contribution from the semiconductor elements (Fig. 5d–f). In the case of Au–Ge NCs, an even larger amount of gold atoms (~98%) was found, which can be related to a strong laser-induced oxidation of Ge nanoclusters, followed by their faster degradation in the aqueous environment. The main reason of the formation of such gold-based nanostructures, which is rarely observed during TEM investigation, can be associated with the considerably different masses (and hence, kinetic energies) of gold and silicon. As a result, at a local point where the concentration of gold nanoclusters is relatively high, they can agglomerate, leading to the formation of the typical Au NPs whose further growth can be restricted by some silicon nanoclusters.

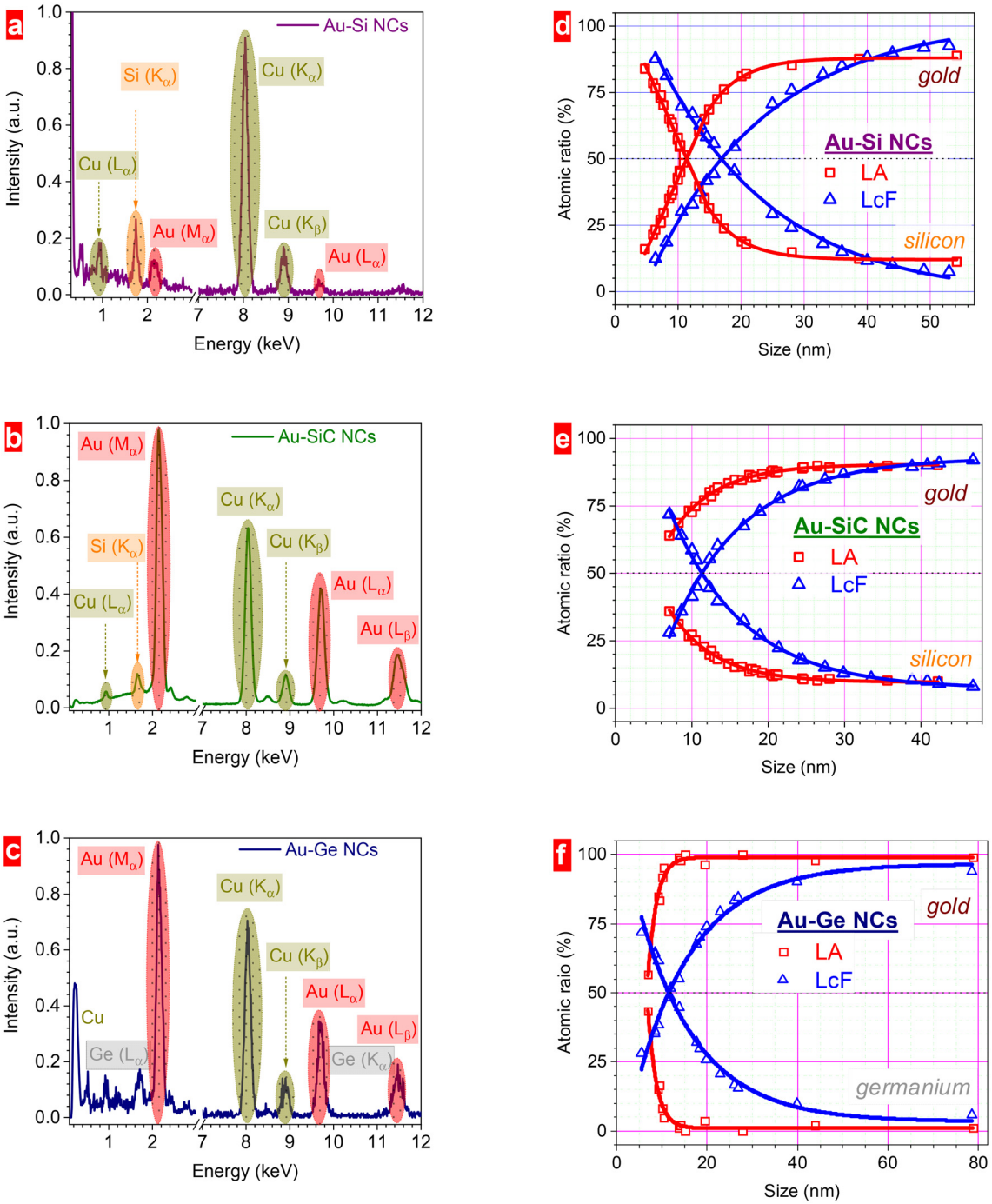

Fig. 5 EDX spectra of: (a) Au–Si NCs, (b) Au-SiC NCs, (c) Au–Ge NCs. Size-dependent chemical composition (atomic ratio) of metallic-semiconductor NCs: (d) Au–Si, (e) Au-SiC, (f) Au–Ge.

However, most NPs (with the mean sizes of ~5–10 nm) have considerably different chemical compositions in comparison with rare large ones (Fig. 5d–f). In this case, the growth of NCs can occur close to the focal point of the laser irradiation, where there is a mixture of gold nanoclusters (ejected from the solid target during the direct LA), and of semiconductor nanoclusters due to the fragmentation of semiconductor NPs (Fig. 4a). Because of a high concentration of different nanoclusters, their kinetic energy can be significantly reduced due to numerous collisions. The latter can more strongly affect the lighter silicon nanoclusters, considerably increasing their local concentration in the plasma plume. Hence, it provokes a strong increase of the Si/Au atomic ratio for smaller NCs due to the further interaction of silicon and gold nanoclusters, forming composite NPs. Moreover, the gold and semiconductor-based plasma plumes can possess different pro-

perties (temperature or pressure distribution), which can also affect the interaction between different elements.

Additionally, one can observe a significant difference between the size-dependent behavior of the chemical composition of Au-SiC and Au–Ge NCs, as compared to the Au–Si ones (Fig. 5d–f). In the case of the Au-SiC nanostructures, this significant difference may be associated with a lower amount of silicon atoms in Au-SiC that also contains carbon atoms. However, we were not able to estimate their amount due to the use of carbon-coated TEM grids. One can hypothesize that the SiC-based nanostructures can have a comparable amount of carbon atoms; thus, the overall contribution of semiconductor elements in the NCs will be similar to the Au–Si ones. Nevertheless, one can also admit some burning of carbon atoms, owing the high-power laser irradiation, which will be additionally studied using X-ray techniques. In the case of Au–Ge NPs, there may be a fast degradation of Ge nanostructures under the high-power laser pulses in oxygen-rich aqueous medium.

It is worth noting that the chosen approach, either direct LA or LcF, also significantly affected the size-dependent composition behaviour (Fig. 5d–f). As suggested above, the laser-generated plasma plumes can be different in the case of direct LA and LcF (Fig. 4). Hence, this can lead to significant variations in their properties, affecting the interaction between gold and semiconductor nanoclusters. In particular, one can have a much more homogeneous distribution between the concentration of gold and semiconductor nanoclusters (formed due to the laser-induced decomposition of Au and semiconductor NPs) as compared to direct LA (Fig. 4). In the LcF case, the size of the plasma plumes can be considerably smaller in contrast to the LA approach, which might further restrict the growth of the NCs (Fig. 3).

Moreover, the PLALs synthesis resulted in a decrease of the hydrodynamic size of the formed NCs. MA-DLS measurements showed that the pure semiconductor NPs possessed higher hydrodynamic sizes (117 nm for Si NPs, 118 nm for SiC NPs, 120 nm for Ge NPs) than pure Au NPs (109 nm). However, further synthesis of plasmonic NCs led to a considerable reduction of the hydrodynamic sizes of NPs, depending on the used technique.

Indeed, in all cases, the NCs prepared by the LcF approach demonstrated much lower hydrodynamic sizes than that formed by the direct LA method (Au–Si: 79 nm *vs.* 104 nm, Au-SiC: 85 nm *vs.* 105 nm, Au–Ge: 77 nm *vs.* 104 nm). Hence, the laser-induced generation of plasmonic semiconductor-based NCs provided up to 35% decrease in the hydrodynamic size of composite NPs in comparison with pure ones (Fig. S3†). It is worth noting that these tendencies fully matched the size behaviour of the plasmonic NCs obtained by electron microscopy (Fig. 3). Thus, the main reason for the decreased hydrodynamic size may be associated with the reduced physical sizes of the NPs. Moreover, the different NC structures formed by the two laser approaches may also be responsible for the reduction of the slipping plane around the NPs.

This laser-induced structural modification also led to a considerable increase of the concentration of NPs in colloidal solutions (Fig. S3d–f†). Firstly, the initial concentration of single-element NPs was $\sim 10^{10}$ NPs per mL for Au NPs and $\sim 5 \times 10^{11}$ NPs per mL for the semiconductor ones. This difference can be explained by (i) the different masses of these elements, and (ii) the different ablation thresholds of the aforementioned materials. Further laser treatment of the colloidal solutions revealed an increase in the concentration of the synthesized composite nanostructures up to $\sim 10^{12}$–10^{13} NPs per mL (Fig. S3d–f†). This can be promoted by the laser-induced fragmentation of the NPs (Fig. S3a–c†), followed by further interaction of gold and the semiconductor nanoclusters (Fig. 4). It is worth noting that the LcF approach formed a ~2-fold greater amount of NCs than the direct LA approach (Fig. S3d–f†). This may be associated with the previously proposed larger number of laser-generated plasma plumes during LcF, where individual NPs affected by the laser irradiation can become a source of the plasma plumes.

The synthesized plasmonic semiconductor-based NCs revealed good chemical stability of the aqueous colloidal solutions, showing high values of the ξ-potential (Fig. S4a–c†). Here, all single-element semiconductor NPs possessed a lower value of the ξ-potential (−30 mV) in comparison with the Au NPs (−38 mV) (Fig. S4a–c†). However, further formation of composite nanostructures changed these values, depending on the chosen PLALs approach. Indeed, all NCs prepared by the direct LA approach demonstrated ξ-potential values close to that of Au NPs. However, the LcF approach led to the highest values of the ξ-potential values, reaching −47 mV for Au–Ge NCs (Fig. S4a–c†). These differences may be a consequence of the various distributions of semiconductor and gold atoms in NCs formed by the two distinct laser approaches.

To study the changes of the electrical conductivity of NPs due to their transformation into a composite form, they were characterized by DLS system and a Hanna conductivity meter. Similar trends were obtained for all plasmonic NCs synthesized using various IV group semiconductors (Fig. S4d–f†). Surprisingly, the conductivity of all pure semiconductor NPs (9.384 μS cm^{-1} for Si NPs, 9.795 μS cm^{-1} for SiC NPs, 10.843 μS cm^{-1} for Ge NPs) were found to be larger than that of pure Au NPs (7.746 μS cm^{-1}) (Fig. S4d–f†). Such an effect can be probably caused by the laser-assisted material nanostructuring, which leads to the size variation of NPs formed from different chemical elements. This considerably affects their electrical conductivity in comparison with bulk materials, depending on the nanostructure size. Nevertheless, the electrical conductivity of all NCs prepared by the LA approach was larger than that of all pure NPs (Fig. S4d–f†), while the electrical conductivity of all LcF-synthesized NCs was similar to the corresponding pure semiconductor NPs (Fig. S4d–f†): (11.988 μS cm^{-1} *vs.* 8.692 μS cm^{-1} for Au–Si NCs, 12.446 μS cm^{-1} *vs.* 8.874 μS cm^{-1} for Au-SiC NCs, 15.129 μS cm^{-1} *vs.* 10.262 μS cm^{-1} for Au–Ge NCs). The better electrical conductivity of all NCs formed by direct LA in comparison with LcF can be mainly explained by the higher content of gold atoms in the case of direct LA, despite their similar sizes (Fig. 5d–f). Moreover, the different structure of NCs or distribution of the

semiconductor and metallic elements may play a significant role, which will be separately studied by means of X-ray and TEM-EDX techniques.

To investigate the plasmonic properties of the metallic-semiconductor NCs, the absorbance spectra of single- and multi-element NPs were analysed. Firstly, the optical properties of the single-element pure semiconductor nanostructures (Si NPs, SiC NPs, Ge NPs) showed no plasmonic features (Fig. 6) that fully correspond to the literature data. However, the laser-synthesized NCs based on all used IV group semiconductors exhibited clear plasmonic responses corresponding to nanostructured gold (Fig. 6). The appearance of the clear plasmonic absorption in the semiconductor-based nanostructures is due to their merging with noble metal nanostructures. It is worth noting that all plasmonic NCs formed by the direct LA approach possessed considerably stronger plasmonic absorption than that prepared by the LcF approach (Fig. 6). Such behaviour may be due to a larger amount of Au atoms in NCs formed by direct LA in comparison with LcF (Fig. 5d–f). The larger absorbance of composite NPs at the violet-blue spectral range as compared to pure ones may be due to the contribution of the semiconductor nanostructures, which show a higher response at this range (Fig. 6).

To study the emission properties from the laser-synthesized plasmonic IV group nanocomposites, their aqueous colloidal solutions were irradiated by UV light (4 eV) provided by a Xe lamp, and the signal was collected through an excitation double monochromator (2 nm bandwidth). Firstly, all spectra demonstrated a sharp feature at ~3.65 eV (340 nm) (Fig. 7) that redshifted with the decrease of the photon energy, accompanied with the exponential reduction of the signal intensity (Fig. 8). To clarify the mechanism of this signal, their PL was further compared with that of the pure deionized water obtained under the same experimental conditions. Evidently, it gave no emission signals in the selected spectral range, except for a similar sharp feature at the same emission photon energy (Fig. S5†). Thus, one can conclude that the signal came from the used liquid medium due to Raman scattering,[48] and can be disregarded from further analysis. Similar to pure water, both semiconductor and gold single-element NPs prepared by IR ps laser ablation in the aqueous environment also demonstrated the absence of any emission signals. This is fully in line with our previous study, where this kind of large NPs exhibited strong nonlinear optical properties without PL due to the absence of quantum confinement of the photo-excited charge carriers.[44,49–51]

Surprisingly, the restructuring provided by the direct LA approach promoted the appearance of a considerable multi-band emission in the blue spectral range for all studied NCs upon excitation by the Xe lamp (Fig. 7). These complex PL spectra were fitted using 5 Gaussian curves, including one for the observed Raman response (Fig. 7). One can distinguish several strong emission bands predominantly in the blue part of the visible range at 3.1–3.4 eV (355–395 nm) and 2.8–3.0 eV (415–445 nm), depending on the used IV group element. Moreover, some weak responses located at 2.1–2.2 eV

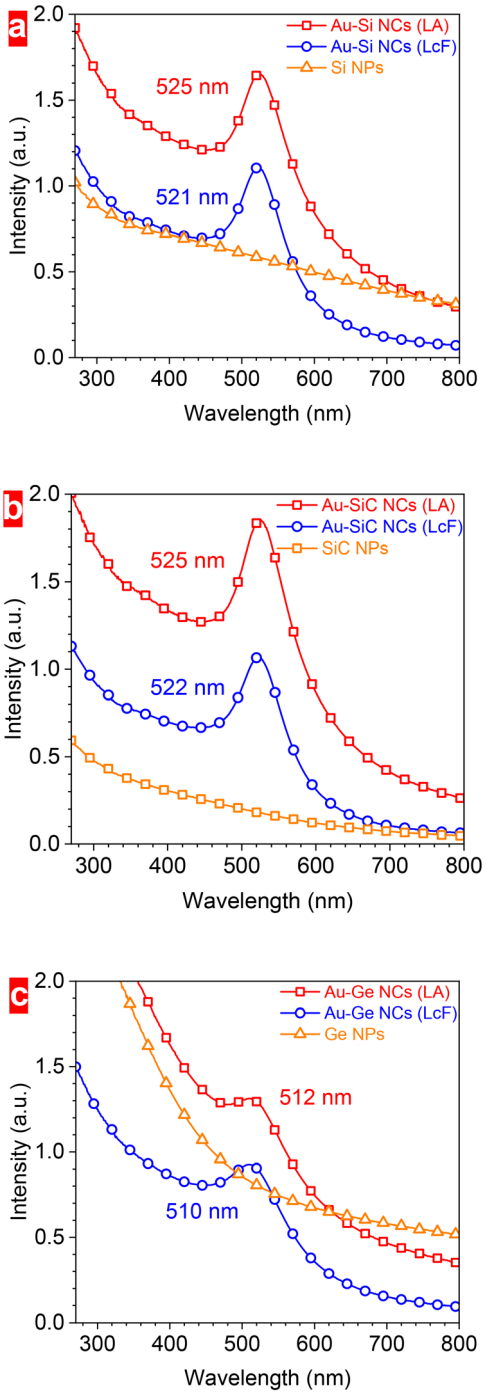

Fig. 6 Absorbance spectra of metallic-semiconductor NCs in comparison with that of corresponding semiconductor NPs: (a) Au–Si; (b) Au-SiC; (c) Au–Ge.

(565–590 nm) and 2.6 eV (475 nm) were identified under these experimental conditions. Thus, one can expect different radiative recombination mechanisms in the laser-synthesized plasmonic NCs, leading to the observed PL bands.

The used laser processing approaches also demonstrated a significant impact on the PL efficiency of all plasmonic NCs, while their spectral positions remained almost the same

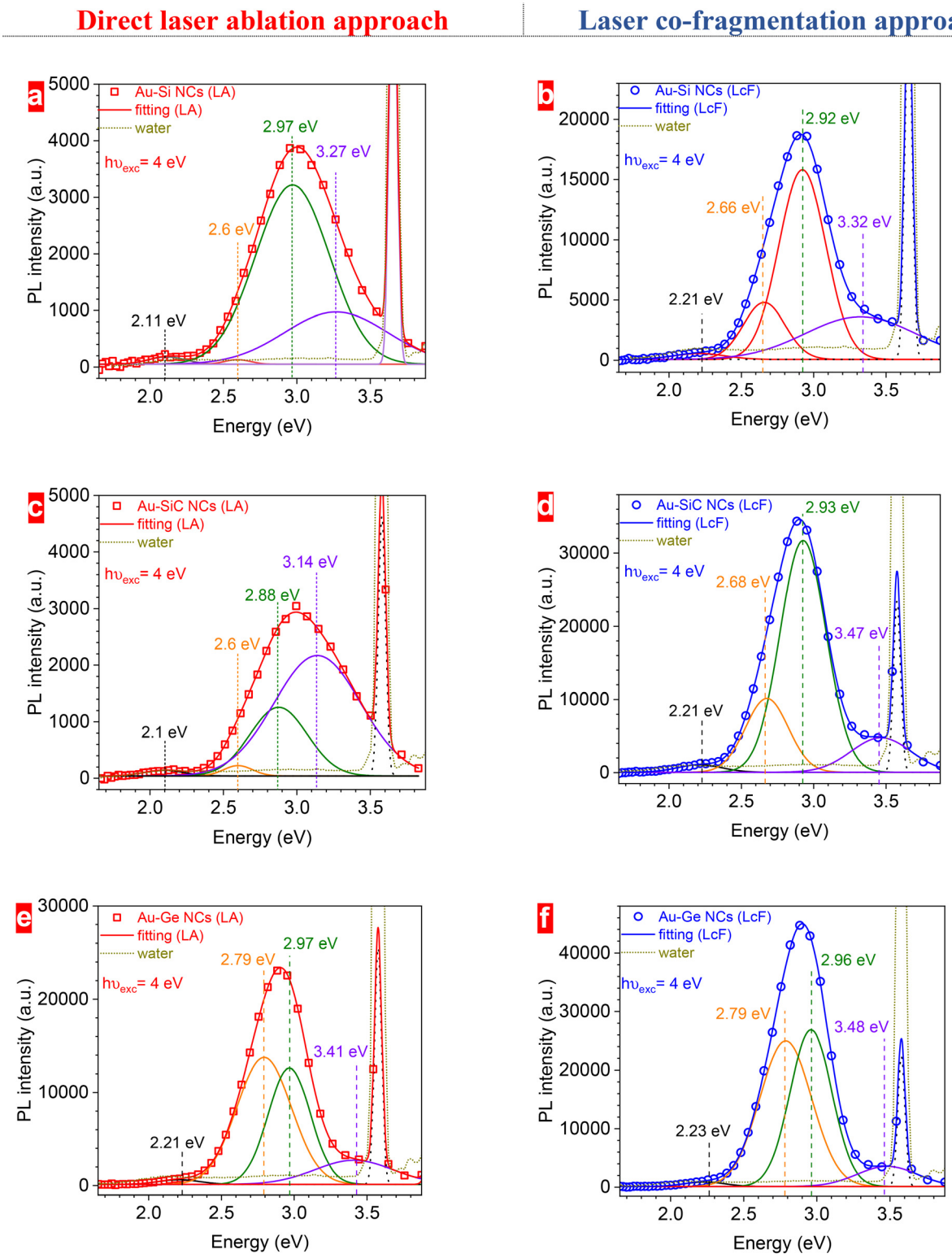

Fig. 7 PL spectra of metallic-semiconductor NCs prepared by LA (a, c and e) and LcF (b, d and f) approaches: (a and b) Au–Si NCs, (c and d) Au-SiC NCs, (e and f) Au–Ge NCs (4 eV excitation photon energy, 1 s acquisition time, 5 scans).

(Fig. 7). All nanocomposites formed by the LcF approach revealed much stronger emission as compared to that prepared by the direct LA technique: 5-fold for Au–Si NCs, 11-fold for Au-SiC NCs, and 2-fold for Au–Ge NCs (Fig. 7 and 8). This can point to the different amounts of centers for radiative recombination in the nanomaterials prepared by the two distinct

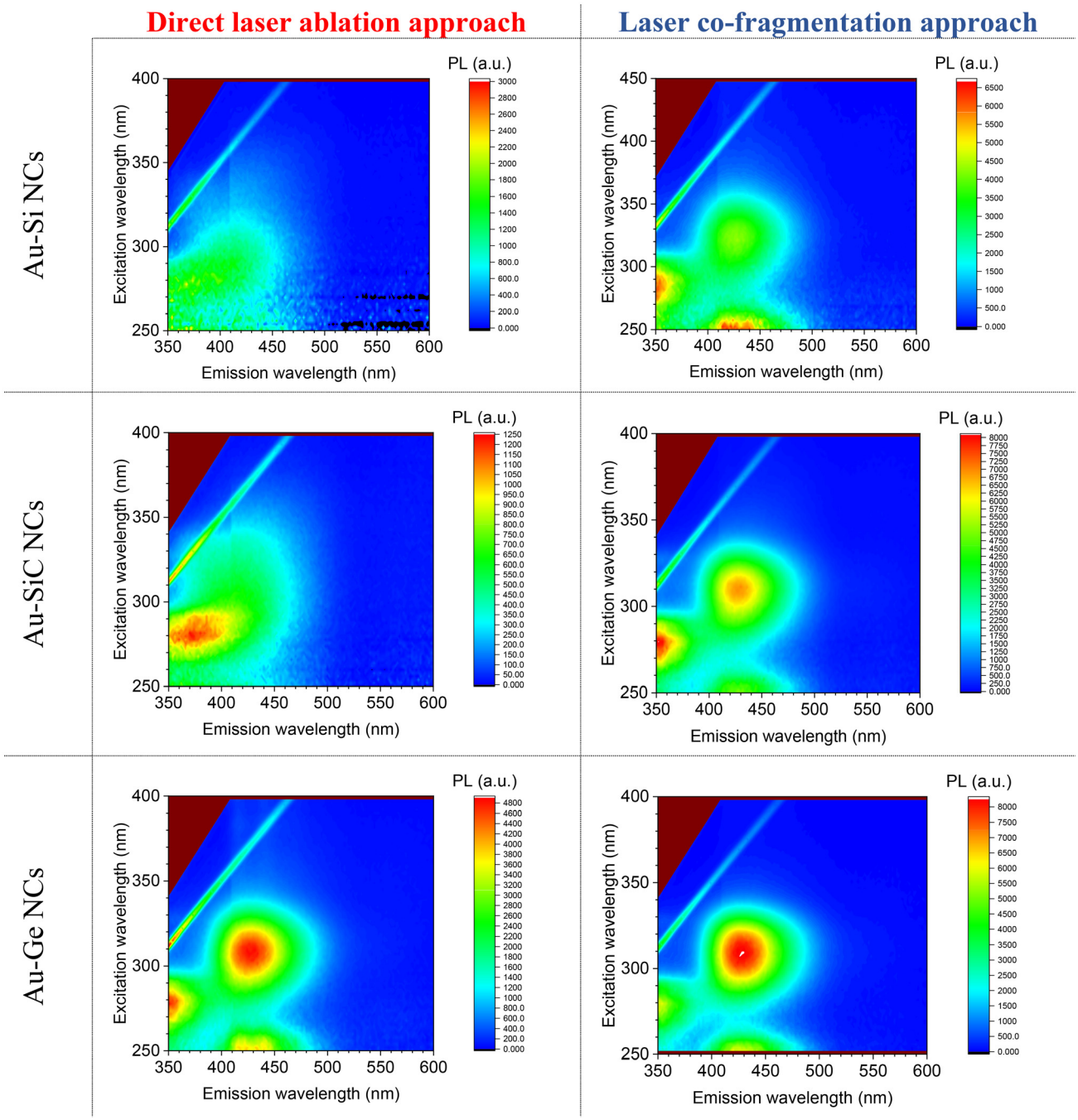

Fig. 8 Excitation–emission PL mapping of plasmonic-semiconductor NCs (1 s acquisition time, 1 scan).

PLALs approaches. This difference can originate from different processes of the interaction between the semiconductor, metallic and oxygen elements in the laser-generated plasma plume. In particular, a more homogeneous spatial distribution of both gold and semiconductor elements during LcF can promote a larger amount of smaller semiconductor nanoclusters, as well as better defect passivation due to bonding with gold. Thus, it can increase the PL efficiency due to (i) the larger amount of radiative recombination channels, and/or (ii) lower probability of non-radiative losses on the surface defects. Moreover, these semiconductor nanodomains may be surrounded by noble metal elements that provide plasmonic enhancement of the radiative recombination channels. Conversely, a larger amount of metal species (Fig. 5) can lead to PL quenching, resulting in weaker emission from all NCs prepared by the LcF approach.[52,53]

When analyzing PL of the low-dimensional semiconductors, *e.g.*, silicon nanostructures, one often considers the excitonic emission of silicon nanocrystallites due to the radiative recombination of photoexcited charge carriers

affected by the quantum confinement effect.[50,51] Here, the size of the nanostructures strongly affects the efficiency and spectral position of the emission.[54] Indeed, smaller nanocrystallites promote higher PL intensity due to the suppression of the non-radiative recombination channel caused by a larger exciton binding energy. At the same time, they also increase the effective bandgap of the semiconductor nanostructures due to a larger quantum confinement contribution. As a result, a blueshift of the spectral position occurs for smaller nanostructures.[54] For instance, 6 nm silicon nanocrystallites exhibit emission at around 1.3 eV, while 2 nm ones emitted at 2.0 eV.[54] Thus, excitonic emission can be responsible for the weak response observed at 2.1–2.2 eV (565–590 nm), which may be associated with the emission from 1.5–1.8 nm nanocrystallites.[54] The PL band located at 3.1–3.4 eV correlates with the emission from small (2–5 nm) alkyl-terminated silicon nanoparticles consisting of ultra-small nanocrystallites.[55]

The origin of the blue emission of plasmonic semiconductor nanocomposites may be associated with the presence of different kinds of suboxides, as it was previously shown for Si/Au NCs formed at different laser ablation times.[56] The mechanism of the blue PL band has been described in detail elsewhere.[57] Briefly, electrons can be excited at different Brillouin points when quantum-sized NPs are excited by the UV irradiation.[57] The presence of the two excitation bands (Fig. 8) may be associated with the $\Gamma_{25} \rightarrow \Gamma_{15}$ or $\Gamma_{25} \rightarrow \Gamma_2$ direct transitions.[57] Afterwards, some excitons can be trapped at different defect levels in the bandgap, associated with either P_b-centers or gold acceptor (E_c–0.55 eV) and donor (E_v + 0.35 eV) states.[56] Other excitons can migrate to the near-interface traps that are related to the oxidized semiconductor nanostructures, with further recombination resulting in the blue emission.[57]

Apart from this, PL bands located at 2.9–3.3 eV can appear from a complex structure formed due to the strong interaction between gold, oxygen and semiconductor atoms, and consisting of small semiconductor nanocrystals in the (sub-)oxide matrix containing metallic impurities. Here, the defect-related PL model (similar to the case of silicon nitride) can be applicable.[58] Such radiative recombination transitions can occur: $Si^0 \rightarrow E_v$ (2.9 eV) or Si–O–Si (2.6–2.7 eV), $E_c \rightarrow Si^0$ (2.1–2.2 eV).[58] Emission peaks at 340, 350 and 370 nm (3.65 eV, 3.54 eV and 3.35 eV) were also observed in thermally oxidized porous silicon, as well as in SiO_2 powder,[59] while radiative transitions at 340 and 440 nm were detected in SiC nanostructures.[60,61] Moreover, germanium nanostructures also exhibited different PL bands in the UV-blue range, in particular, at 460 nm (2.7 eV) and 540 nm (2.3 eV).[62,63]

With the aim of further hyperthermia applications, the heating efficiency of gold-semiconductor NCs was assessed using IR (800 nm) laser irradiation. For this purpose, 1 mL of the aqueous colloidal solutions of plasmonic NCs were firstly stabilized at room temperature (~24 °C) prior to the experiments. Afterwards, they were continuously irradiated by fs laser pulses for 600 s, and the temperature of the colloidal solutions was detected by a thermal camera. The laser irradiation absorbed by the plasmonic NCs was converted into heat, similar to the previously described effect.[41,64] The fs laser irradiation provided a considerable heating of the colloidal solutions, which strongly depended on the (i) irradiation duration, (ii) chosen laser processing approach, and (iii) chemical composition of NCs (Fig. S6†). Moreover, one can highlight the more inhomogeneous temperature distribution of the colloids formed by the direct LA, which was the most pronounced for the Au–Ge nanostructures (Fig. S6†).

A longer laser impact on the colloidal solutions evidently led to higher temperature, which gradually increased with the irradiation duration (Fig. S6† and Fig. 9). Being irradiated for 120 s, the temperature of the plasmonic NCs prepared by direct LA approach increased by the following values: Au–Si – 4.7 °C, Au-SiC – 2.8 °C and Au–Ge – 7 °C (Fig. S6† and Fig. 9). The highest temperature difference achieved after 600 s laser irradiation was: Au–Si – 8.7 °C, Au-SiC – 6.5 °C and Au–Ge – 11.9 °C (Fig. S6† and Fig. 9). Moreover, the used laser processing approaches remarkably affected the laser-induced heating rate and the maximum achieved temperature. Indeed, all plasmonic NCs synthesized by the LcF approach achieved a lower temperature in comparison with the LA ones, despite being irradiated for the same duration (Fig. 9). NCs synthesized *via* LcF approach exhibited temperature differences of 1.8 °C (Au–Si), 2.2 °C (Au-SiC) and 3.4 °C (Au–Ge) after 120 s of the fs laser irradiation, and their maximum temperature difference after 600 s irradiation was 5.2 °C (Au–Si), 5.1 °C (Au-SiC) and 8.8 °C (Au–Ge) (Fig. 9).

The different heating rate and temperature distribution of the laser-generated colloidal solutions containing diverse plasmonic nanostructures can be explained by the influence of their different structure and chemical composition on their thermal properties. Firstly, all IV group semiconductor materials possess various specific heat capacity values: Si – 710 J $(kg\ K)^{-1}$, C – 710 J $(kg\ K)^{-1}$ and Ge – 321 J $(kg\ K)^{-1}$.[65] Thus, pure Si and SiC-based NPs ought to have similar heating rates that should be smaller than that of Ge NPs. Secondly, gold has the lowest specific heat capacity value $\{129\ J\ (kg\ K)^{-1}\}$ among all used elements.[65] Hence, its presence in the composite nanostructures should decrease their specific heat capacity and ensure a faster heating of the plasmonic NCs, as compared to pure semiconductor NPs. The increased gold content should also contribute to the higher temperature of the studied system.

Indeed, all nanocomposites formed by the direct LA approach revealed a faster heating of the colloidal solutions, achieving higher temperature as compared to the LcF one (Fig. 9). According to the EDX data (Fig. 5d and e), all LA-formed NCs possessed a larger amount of gold atoms in comparison with the LcF ones, confirming the aforementioned hypothesis. Moreover, the various relative distributions of semiconductor, gold and oxygen elements in NCs prepared by different laser processing approaches can also affect their heating efficiency, which will be studied separately. At the same time, Au-SiC nanostructures are expected to be heated more than Au–Si ones due to the larger concentration of gold

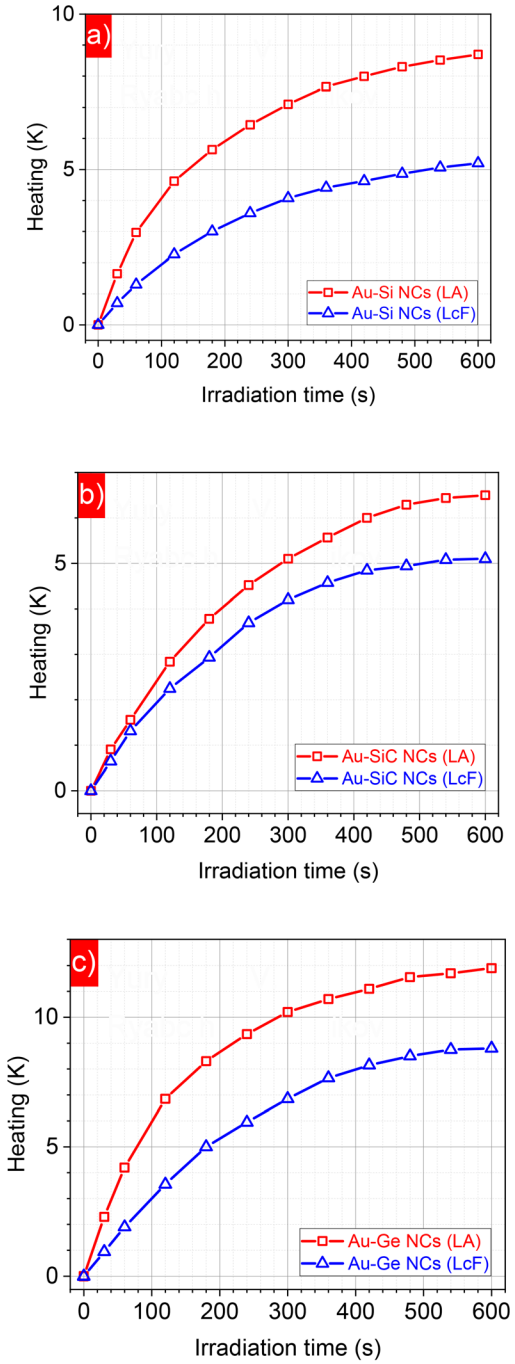

Fig. 9 Laser irradiation time-dependent heating of (a) Au–Si NCs, (b) Au-SiC NCs, and (c) Au–Ge NCs.

atoms. However, the EDX results did not detect the content of carbon atoms in Au-SiC NCs, leading to a remarkable deviation of the laser-induced heating results. From this contradiction, one can expect a considerable number of carbon atoms, leading to a much lower contribution of gold ones that must be verified using other techniques.

The stronger heating of Au–Ge nanomaterials as compared to silicon-based ones can be explained by (i) the lower specific heat capacity value of Ge in comparison with other semiconductor elements, and (ii) the greater amount of gold atoms. The impact of the PLALs approach on the laser-induced heating of plasmonic-semiconductor NCs can be due to different mechanisms of the interaction between gold, oxygen and semiconductor elements, which will affect the structure of NCs, and hence, their thermal properties. To establish the mechanisms of these differences, a deeper study of the structural and thermal properties of composite nanostructures is required, which is beyond the scope of the current paper.

The inhomogeneous temperature distribution of Au–Ge NCs in comparison with plasmonic silicon-based ones may be due to the different values of their thermal conductivity. The thermal conductivity of bulk gold and semiconductors of the IV group is high (Au – 320 W (m K)$^{-1}$; Si – 150 W (m K)$^{-1}$; C – 140 W (m K)$^{-1}$; Ge – 60 W (m K)$^{-1}$),[66] contrary to that of water (0.6 W (m K)$^{-1}$). However, the nanostructuring performed in the oxygen-rich medium considerably reduces their thermal conductivity values, which depend on the size, shape and oxidation rate of the nanostructures. In general, the thermal conductivity of germanium decreases towards ~40 W (m K)$^{-1}$,[67] while that of silicon is reduced to ~1–7 W (m K)$^{-1}$.[68] Thus, the discrepancy in the thermal conductivity values of the nanostructures and their liquid environment may lead to the inhomogeneous heat dissipation. Hence, the used laser processing approach can significantly affect the laser-induced heating of multi-element nanostructures, being also dependent on the used IV group semiconductor elements.

Thus, ultrafast laser processing is a very efficient way to extend the semiconductor nanostructure performance by merging with various metallic elements. The designed plasmonic-fluorescent nanocomposites are very promising for employment in different life science applications. Moreover, their production rate can be easily up-scaled *via* diffraction optical elements (DOE) and/or flow chambers, allowing the synthesis of a large amount of the required multi-modal nanostructures.

Conclusions

In summary, plasmonic nanocomposites were formed by different ultrafast laser processing approaches in liquids using various IV group semiconductor (Si, SiC, Ge) nanostructures. All laser-synthesized NCs revealed efficient multi-band blue (420 nm) photoluminescence, which was considerably stronger for the LcF nanostructures. They also revealed strongly size-dependent chemical compositions, which were more pronounced for the LcF approach compared to direct LA. Higher concentrations (~10^{12} NPs per mL) of smaller (~7 nm) ligand-free composite NPs were also provided, showing their better stability in aqueous medium (up to −47 mV). Furthermore, the direct LA technique led to a better electrical conductivity (up to 15.129 μS cm^{-1}) and considerably stronger (~70%) plasmonic absorbance of the NCs due to the higher content of gold atoms. The latter also ensured the more remarkable fs laser-induced heating efficiency (up to 80%) of all plasmonic NCs

synthesized by the direct LA approach. These findings will contribute toward the laser synthesis of composite multi-modal nanostructures that can be employed for different healthcare applications, such as optical biosensing, bioimaging and hyperthermia, as well as considerably simplify protocols to expand the performance of single-element NPs employed in healthcare applications.

Data availability

All relevant data are included in the paper and the ESI.† Open access data are available here: **https://doi.org/10.57680/asep.0598646**.

Conflicts of interest

There are no conflicts to declare.

Acknowledgements

This project has received funding from the European Union's Horizon 2020 research and innovation programme under the Marie Skłodowska-Curie grant agreement, No. 897231 (LaDeNTher). We are also thankful to the European Regional Development Fund, and for support from OPJAK financed by ESIF and the Czech MEYS (Project No. SenDiSo – CZ.02.01.01/00/22_008/0004596).

References

1 D. Yang, Z. Cui, Z. Wen, Z. Piao, H. He, X. Wei, L. Wang, S. Mei, W. Zhang and R. Guo, Recent Updates on Functionalized Silicon Quantum-Dot-Based Nanoagents for Biomedical Applications, *ACS Mater. Lett.*, 2023, **5**(4), 985–1008, DOI: **10.1021/acsmaterialslett.2c01225**.

2 B. Xu, S. Li, R. Shi and H. Liu, Multifunctional mesoporous silica nanoparticles for biomedical applications, *Signal Transduction Targeted Ther.*, 2023, **8**, 435, DOI: **10.1038/s41392-023-01654-7**.

3 J.-H. Park, L. Gu, G. von Maltzahn, E. Ruoslahti, S. N. Bhatia and M. J. Sailor, Biodegradable luminescent porous silicon nanoparticles for *in vivo* applications, *Nat. Mater.*, 2009, **8**, 331–336, DOI: **10.1038/nmat2398**.

4 Yu. V. Ryabchikov, I. A. Belogorokhov, M. B. Gongalskiy, L. A. Osminkina and V. Yu. Timoshenko, Photosensitized Generation of Singlet Oxygen in Powders and Aqueous Suspensions of Silicon Nanocrystals, *Semiconductors*, 2011, **45(8)**, 1059–1063, DOI: **10.1134/S106378261108015X**.

5 E. A. Konstantinova, V. A. Demin, A. S. Vorontzov, Yu. V. Ryabchikov, I. A. Belogorokhov, L. A. Osminkina, P. A. Forsh, P. K. Kashkarov and V. Yu. Timoshenko, Electron Paramagnetic Resonance and Photoluminescence Study of Si Nanocrystals – Photosensitizers of Singlet Oxygen Molecules, *J. Non-Cryst. Solids*, 2006, **352**(9–20), 1156–1159, DOI: **10.1016/j.jnoncrysol.2005.12.017**.

6 Yu. V. Ryabchikov, I. A. Belogorokhov, A. S. Vorontsov, L. A. Osminkina, V. Yu. Timoshenko and P. K. Kashkarov, Dependence of the Singlet Oxygen Photosensitization Efficiency on Morphology of Porous Silicon, *Phys. Status Solidi A*, 2007, **204**(5), 1271–1275, DOI: **10.1002/pssa.200674306**.

7 H. Zhao, Y. Li, J. Chen, J. Zhang, Q. Yang, J. Cui, A. Shi and J. Wu, Environmental stimulus-responsive mesoporous silica nanoparticles as anticancer drug delivery platforms, *Colloids Surf., B*, 2024, **234**, 113758, DOI: **10.1016/j.colsurfb.2024.113758**.

8 P. V. Maximchik, K. Tamarov, E. V. Sheval, E. Tolstik, T. Kirchberger-Tolstik, Z. Yang, V. Sivakov, B. Zhivotovsky and L. A. Osminkina, Biodegradable Porous Silicon Nanocontainers as an Effective Drug Carrier for Regulation of the Tumor Cell Death Pathways, *ACS Biomater. Sci. Eng.*, 2019, **5**(11), 6063–6071, DOI: **10.1021/acsbiomaterials.9b01292**.

9 H. Kirla, D. J. Henry, S. Jansen, P. L. Thompson and J. Hamzah, Use of Silica Nanoparticles for Drug Delivery in Cardiovascular Disease, *Clin. Ther.*, 2023, **45**(11), 1060–1068, DOI: **10.1016/j.clinthera.2023.08.017**.

10 R. S. Soumya and K. G. Raghu, Recent advances on nanoparticle-based therapies for cardiovascular diseases, *J. Cardiol.*, 2023, **81**(1), 10–18, DOI: **10.1016/j.jjcc.2022.02.009**.

11 S. Saeed, S. R. U. Din, S. U. Khan, R. Gul, F. A. Kiani, A. Wahab and M. Zhong, Nanoparticle: A Promising Player in Nanomedicine and its Theranostic Applications for the Treatment of Cardiovascular Diseases, *Curr. Probl. Cardiol.*, 2023, **48**(5), 101599, DOI: **10.1016/j.cpcardiol.2023.101599**.

12 J. K. Alagarasan, S. Shasikala, S. Ganesan, M. Arunachalam, U. Manojkumar, S. Palaninaicker, D. D. Nguyen, S. W. Chang, M. Lee and H.-M. Lo, Silicon nanoparticles as a fluorometric probe for sensitive detection of cyanide ion and its application in C. elegans bioimaging, *Environ. Res.*, 2023, **224**, 115402, DOI: **10.1016/j.envres.2023.115402**.

13 S. V. Zabotnov, A. V. Skobelkina, E. A. Sergeeva, D. A. Kurakina, A. V. Khilov, F. V. Kashaev, T. P. Kaminskaya, D. E. Presnov, P. D. Agrba, D. V. Shuleiko, P. K. Kashkarov, L. A. Golovan and M. Yu. Kirillin, Nanoparticles Produced via Laser Ablation of Porous Silicon and Silicon Nanowires for Optical Bioimaging, *Sensors*, 2020, **20**(17), 4874, DOI: **10.3390/s20174874**.

14 J. Sobhanan, K. Ono, T. Okamoto, M. Sawada, P. S. Weiss and V. Biju, Photosensitizer-singlet oxygen sensor conjugated silica nanoparticles for photodynamic therapy and bioimaging, *Chem. Sci.*, 2024, **15**, 2007–2018, DOI: **10.1039/D3SC03877G**.

15 M. Yu. Kirillin, E. A. Sergeeva, P. D. Agrba, A. D. Krainov, A. A. Ezhov, D. V. Shuleiko, P. K. Kashkarov and S. V. Zabotnov, Laser-ablated silicon nanoparticles: optical

properties and perspectives in optical coherence tomography, *Laser Phys.*, 2015, **25**, 075604, DOI: **10.1088/1054-660X/25/7/075604**.

16 S. V. Zabotnov, F. V. Kashaev, D. V. Shuleiko, M. B. Gongalsky, L. A. Golovan, P. K. Kashkarov, D. A. Loginova, P. D. Agrba, E. A. Sergeeva and M. Yu. Kirillin, Silicon nanoparticles as contrast agents in the methods of optical biomedical diagnostics, *Quantum Electron.*, 2017, **47**, 638, DOI: **10.1070/QEL16380**.

17 T. Ming, B. Dietzek-Ivanšić, X. Lu, X. Zuo and V. Sivakov, Silicon Nanowires Decorated with Silver Nanoparticles for Photoassisted Hydrogen Generation, *ACS Appl. Energy Mater.*, 2022, **5**(6), 7466–7472, DOI: **10.1021/acsaem.2c00968**.

18 T. Ming, S. Turishchev, A. Schleusener, E. Parinova, D. Koyuda, O. Chuvenkova, M. Schulz, B. Dietzek and V. Sivakov, Silicon Suboxides as Driving Force for Efficient Light-Enhanced Hydrogen Generation on Silicon Nanowires, *Small*, 2021, **17**(8), 2007650, DOI: **10.1002/smll.202007650**.

19 Yu. V. Ryabchikov, V. Lysenko and T. Nychyporuk, Enhanced Thermal Sensitivity of Silicon Nanoparticles Embedded in (nano–Ag)/SiNx for Luminescent Thermometry, *J. Phys. Chem. C*, 2014, **118**, 12515–12519, DOI: **10.1021/jp411887s**.

20 Yu. V. Ryabchikov, S. A. Alekseev, V. Lysenko and G. Bremond, J–M. Bluet. Photoluminescence thermometry with alkyl–terminated silicon nanoparticles dispersed in low–polar liquids, *Phys. Status Solidi RRL*, 2013, **7(6)**, 414–417, DOI: **10.1002/pssr.201307093**.

21 P. Larissa, B. Gambrill, R. D. P. de Carvalho, M. Z. D. Picolo, V. Cavalli, L. C. C. Boaro, P. Prokopovich and K. Cogo-Müller, Development, characterization and antimicrobial activity of multilayer silica nanoparticles with chlorhexidine incorporated into dental composites, *Dent. Mater.*, 2023, **39**(5), 469–477, DOI: **10.1016/j.dental.2023.03.005**.

22 A. Shirmohammadi, S. M. Dizaj, S. Sharifi, S. Fattahi, R. Negahdari, M. A. Ghavimi and M. Y. Memar, Promising Antimicrobial Action of Sustained Released Curcumin-Loaded Silica Nanoparticles against Clinically Isolated Porphyromonas gingivalis, *Diseases*, 2023, **11**(1), 48, DOI: **10.3390/diseases11010048**.

23 M. Sultan, A. A. Abdelhakim, M. Nassar and Y. R. Hassan, Active packaging of chitosan film modified with basil oil encapsulated in silica nanoparticles as an alternate for plastic packaging materials, *Food Biosci.*, 2023, **51**, 102298, DOI: **10.1016/j.fbio.2022.102298**.

24 M. M. Lazarević, N. L. Ignjatović, Q. Mahlet, V. V. Bumah, M. Radunović, J. Milašin, D. P. Uskoković and V. Uskoković, Biocompatible Germanium-Doped Hydroxyapatite Nanoparticles for Promoting Osteogenic Differentiation and Antimicrobial Activity, *ACS Appl. Nano Mater.*, 2024, 7(8), 8580–8592, DOI: **10.1021/acsanm.3c05974**.

25 S. A. A. Gaber, A. H. Hamza, M. A. Tantawy, E. A. Toraih and H. H. Ahmed, Germanium Dioxide Nanoparticles Mitigate Biochemical and Molecular Changes Characterizing Alzheimer's Disease in Rats, *Pharmaceutics*, 2023, **15**(5), 1386, DOI: **10.3390/pharmaceutics15051386**.

26 P. He, G. Chen, M. Huang, L. Jing, W. Wu, H.-C. Kuo, C.-C. Tu and S.-L. Chen, Biodegradable germanium nanoparticles as contrast agents for near-infrared-II photoacoustic imaging, *Nanoscale*, 2023, **15**, 11544–11559, DOI: **10.1039/D3NR01594G**.

27 G. Redondo-Fernandez, J. C. Canga, A. Soldado, J. R. Encinar and J. M. Costa-Fernandez, Functionalized heteroatom-doped carbon dots for biomedical applications: A review, *Anal. Chim. Acta*, 2023, **1284**, 341874, DOI: **10.1016/j.aca.2023.341874**.

28 H.-L. Yang, L.-F. Bai, Z.-R. Geng, H. Chen, L.-T. Xu, Y.-C. Xie, D.-J. Wang, H.-W. Gu and X.-M. Wang, Carbon quantum dots: Preparation, optical properties, and biomedical applications, *Mater. Today Adv.*, 2023, **18**, 100376, DOI: **10.1016/j.mtadv.2023.100376**.

29 M. Qasim, A. N. Clarkson and S. F. R. Hinkley, Green Synthesis of Carbon Nanoparticles (CNPs) from Biomass for Biomedical Applications, *Int. J. Mol. Sci.*, 2023, **24**(2), 1023, DOI: **10.3390/ijms24021023**.

30 L. Yang, X. Ding and Y. Zhou, Femtosecond laser induced periodic nanostructures towards enhanced anti-corrosive property of titanium, *Surf. Coat. Technol.*, 2023, **463**, 129533, DOI: **10.1016/j.surfcoat.2023.129533**.

31 T. Nawaz, A. Ali, S. Ahmad, P. Piatkowski and A. S. Alnase, Enhancing Anticorrosion Resistance of Aluminum Alloys Using Femtosecond Laser-Based Surface Structuring and Coating, *Nanomaterials*, 2023, **13**(4), 644, DOI: **10.3390/nano13040644**.

32 M. Liang, Y. Yuan, X. Li, J. Cheng, X. Zhang, K. Zhang and R. You, Enhanced corrosion resistance of Mg and Mg alloys with fs-laser printed hydrophobic and periodically microrippled surface for armor application, *Appl. Surf. Sci.*, 2023, **639**, 158156, DOI: **10.1016/j.apsusc.2023.158156**.

33 S. V. Zabotnov, L. A. Golovan, I. A. Ostapenko, Yu. V. Ryabchikov, A. V. Chervyakov, V. Yu. Timoshenko and P. K. Kashkarov, Femtosecond Nanostructuring of Silicon Surfaces, *JETP Lett.*, 2006, **83**(2), 69–71, DOI: **10.1134/S0021364006020056**.

34 B. A. Bastug, A. Gulsaran, J. R. Pennings, R. Karimi, A. A. Belgabad, A. H. Xu, L. Zaidan, S. Kocer, J. Sanderson, M. Bajcsy, M. Pope and M. Yavuz, Core-Shell, Defective TiO_2 Nanoparticles by Femtosecond Laser Irradiation with Enhanced Photocatalytic Performance, *Mater. Adv.*, 2023, **4**, 1297–1305, DOI: **10.1039/D3MA00019B**.

35 Y. Song, J. Xu, X. Li, A. Zhang and Y. Cheng, Energy-dependent correlation between micro/nano-morphology and stress state of femtosecond laser-induced modification in fused silica, *Opt. Laser Technol.*, 2024, **176**, 110901, DOI: **10.1016/j.optlastec.2024.110901**.

36 R.-R. Xie, H. Zhu, R. Xing, L. Chu, Z. Wang, R. Xia, W. Zhao, Y. Jia, Y. Chen, S. Juodkazis and F. Chen, Femtosecond laser modification of vanadium dioxide for

color display applications, *Appl. Phys. Lett.*, 2023, **123**, 093101, DOI: 10.1063/5.0166212.

37 M. Zukerstein, V. P. Zhukov, Y. P. Meshcheryakov and N. M. Bulgakova, From Localized Laser Energy Absorption to Absorption Delocalization at Volumetric Glass Modification with Gaussian and Doughnut-Shaped Pulses, *Photonics*, 2023, **10**(8), 882, DOI: 10.3390/photonics10080882.

38 E. N. Gerasimova, E. Uvarov, V. V. Yaroshenko, O. Epifanovskaya, A. Shakirova, L. S. Logunov, O. Vlasova, A. Parodi, A. A. Zamyatnin, A. S. Timin, S. V. Makarov and M. V. Zyuzin, Single-Step Fabrication of Resonant Silicon–Gold Hybrid Nanoparticles for Efficient Optical Heating and Nanothermometry in Cells, *ACS Appl. Nano Mater.*, 2023, **6**(20), 18848–18857, DOI: 10.1021/acsanm.3c03189.

39 M. Flimelova, Yu. V. Ryabchikov, J. Behrends and N. M. Bulgakova, Environmentally Friendly Improvement of Plasmonic Nanostructure Functionality towards Magnetic Resonance Applications, *Nanomaterials*, 2023, **13**(4), 764, DOI: 10.3390/nano13040764.

40 Yu. V. Ryabchikov, Facile Laser Synthesis of Multimodal Composite Silicon/Gold Nanoparticles with Variable Chemical Composition, *J. Nanopart. Res.*, 2019, **21**(4), 85, DOI: 10.1007/s11051-019-4523-4.

41 S. O. Gurbatov, V. Puzikov, D. Storozhenko, E. Modin, E. Mitsai, A. Cherepakhin, A. Shevlyagin, A. V. Gerasimenko, S. A. Kulinich and A. A. Kuchmizhak, Multigram-Scale Production of Hybrid Au-Si Nanomaterial by Laser Ablation in Liquid (LAL) for Temperature-Feedback Optical Nanosensing, Light-to-Heat Conversion, and Anticounterfeit Labeling, *ACS Appl. Mater. Interfaces*, 2023, **15**(2), 3336–3347, DOI: 10.1021/acsami.2c18999.

42 Yu. V. Ryabchikov, Multi-modal Laser-Fabricated Nanocomposites with Non-Invasive Tracking Modality and Tuned Plasmonic Properties, *Crystals*, 2023, **13**(9), 1381, DOI: 10.3390/cryst13091381.

43 Yu. V. Ryabchikov and J. Behrends, Expedient Paramagnetic Properties of Surfactant-Free Plasmonic Silicon-Based Nanoparticles, *Opt. Quantum Electron.*, 2020, **52**, 177, DOI: 10.1007/s11082-020-02297-6.

44 Yu. V. Ryabchikov, Size Modification of Optically Active Contamination-Free Silicon Nanoparticles with Paramagnetic Defects by Their Fast Synthesis and Dissolution, *Phys. Status Solidi*, 2019, **216**(2), A1800685, DOI: 10.1002/pssa.201800685.

45 K. W. Kolasinski, M. C. Gupta and L. V. Zhigilei, Plume and Nanoparticle Formation During Laser Ablation, in *Encyclopedia of Interfacial Chemistry: Surface Science and Electrochemistry*, ed. K. Wandelt, Elsevier, Oxford, 2018, vol. 2, pp. 594–603. DOI: 10.1016/B978-0-12-409547-2.14045-4.

46 T. E. Itina, On Nanoparticle Formation by Laser Ablation in Liquids, *J. Phys. Chem. C*, 2011, **115**(12), 5044–5048, DOI: 10.1021/jp1090944.

47 K. Maximova, A. Aristov, M. Sentis and A. V. Kabashin, Size-controllable synthesis of bare gold nanoparticles by femtosecond laser fragmentation in water, *Nanotechnology*, 2015, **26**(6), 065601, DOI: 10.1088/0957-4484/26/6/065601.

48 A. Kalita, K. Deka and M. P. C. Kalita, On the influence of Raman scattering of water in the photoluminescence measurement of water dispersed ZnO nanocrystals, *Methods Appl. Fluoresc.*, 2017, **5**, 027001, DOI: 10.1088/2050-6120/aa6ab8.

49 A. Yu. Kharin, V. V. Lysenko, A. Rogov, Yu. V. Ryabchikov, A. Geloen, I. Tishchenko, O. Marty, P. G. Sennikov, R. A. Kornev, I. N. Zavestovskaya, A. V. Kabashin and V. Yu. Timoshenko, Bi-modal nonlinear optical contrast from Si nanoparticles for cancer theranostics, *Adv. Opt. Mater.*, 2019, **7**(13), 18011728, DOI: 10.1002/adom.201801728.

50 A. G. Cullis, L. T. Canham and P. D. J. Calcott, The structural and luminescence properties of porous silicon, *J. Appl. Phys.*, 1997, **82**(3), 909–965, DOI: 10.1063/1.366536.

51 W. Theiß, Optical properties of porous silicon, *Surf. Sci. Rep.*, 1997, **29**(3–4), 91–192, DOI: 10.1016/S0167-5729(96)00012-X.

52 M. R. Singh, J. Guo, E. Fanizza and M. Dubey, Anomalous Photoluminescence Quenching in Metallic Nanohybrids, *J. Phys. Chem. C*, 2019, **123**, 10013, DOI: 10.1021/acs.jpcc.9b00352.

53 I. J. Kim, Y. Xu and K. H. Nam, Metal-Induced Fluorescence Quenching of Photoconvertible Fluorescent Protein DendFP, *Molecules*, 2022, **27**(9), 2922, DOI: 10.3390/molecules27092922.

54 Y. Yu, G. Fan, A. Fermi, R. Mazzaro, V. Morandi, P. Ceroni, D.-M. Smilgies and B. A. Korgel, Size-Dependent Photoluminescence Efficiency of Silicon Nanocrystal Quantum Dots, *J. Phys. Chem. C*, 2017, **121**(41), 23240–23248, DOI: 10.1021/acs.jpcc.7b08054.

55 C.-S. Yang, R. A. Bley, S. M. Kauzlarich, H. W. H. Lee and G. R. Delgado, Synthesis of Alkyl-Terminated Silicon Nanoclusters by a Solution Route, *J. Am. Chem. Soc.*, 1999, **121(22)**, 5191–5195, DOI: 10.1021/ja9828509.

56 Yu. V. Ryabchikov, I. Mirza, M. Flimelová, A. Kana and O. Romanyuk, Merging of Bi-Modality of Ultrafast Laser Processing: Heating of Si/Au Nanocomposite Solutions with Controlled Chemical Content, *Nanomaterials*, 2024, **14**(4), 321, DOI: 10.3390/nano14040321.

57 S. Yang, W. Li, B. Cao, H. Zeng and W. Cai, Origin of Blue Emission from Silicon Nanoparticles: Direct Transition and Interface Recombination, *J. Phys. Chem. C*, 2011, **115**(43), 21056–21062, DOI: 10.1021/jp2075836.

58 Yu. V. Ryabchikov, Plasmon-affected luminescent nanothermometry with multi-band SiNPs/SiN_X nanocomposites, *J. Lumin.*, 2023, **260**, 119891, DOI: 10.1016/j.jlumin.2023.119891.

59 G. G. Qin, J. Lin, J. Q. Duan and G. Q. Yao, A comparative study of ultraviolet emission with peak wavelengths around 350 nm from oxidized porous silicon and that from SiO_2 powder, *Appl. Phys. Lett.*, 1996, **69**, 1689–1691, DOI: 10.1063/1.117029.

60 C. H. Liang, G. W. Meng, L. D. Zhang, Y. C. Wu and Z. Cui, Large-scale synthesis of β-SiC nanowires by using mesoporous silica embedded with Fe nanoparticles, *Chem. Phys.*

Lett., 2000, **329**(3–4), 323–328, DOI: **10.1016/S0009-2614(00)01023-X**.

61 S. Askari, A. U. Haq, M. Macias-Montero, I. Levchenko, F. Yu, W. Zhou, K. Ostrikov, P. Maguire, V. Svrcek and D. Mariotti, Ultra-small photoluminescent silicon-carbide nanocrystals by atmospheric-pressure plasmas, *Nanoscale*, 2016, **8**, 17141–17149, DOI: **10.1039/C6NR03702J**.

62 D. Carolan and H. Doyle, Size and emission color tuning in the solution phase synthesis of highly luminescent germanium nanocrystals, *J. Mater. Chem. C*, 2014, **2**, 3562–3568, DOI: **10.1039/C4TC00319E**.

63 N. Shirahata, D. Hirakawa, Y. Masuda and Y. Sakka, Size-Dependent Color Tuning of Efficiently Luminescent Germanium Nanoparticles, *Langmuir*, 2013, **29**(24), 7401–7410, DOI: **10.1021/la303482s**.

64 S. O. Gurbatov, A. Yu. Zhizhchenko, V. Yu. Nesterov, E. B. Modin, S. V. Zabotnov and A. A. Kuchmizhak, Au–Si Nanocomposites with High Near-IR Light-to-Heat Conversion Efficiency via Single-Step Reactive Laser Ablation of Porous Silicon for Theranostic Applications, *ACS Appl. Nano Mater.*, 2024, **7**(9), 10779–10786, DOI: **10.1021/acsanm.4c01289**.

65 **https://periodictable.com/Properties/A/SpecificHeat.an.html**.

66 **https://periodictable.com/Properties/A/ThermalConductivity.html**.

67 S. Chae, K. A. Mengle, R. Lu, A. Olvera, N. Sanders, J. Lee, P. F. P. Poudeu, J. T. Heron and E. Kioupakis, Thermal conductivity of rutile germanium dioxide, *Appl. Phys. Lett.*, 2020, **117**, 102106, DOI: **10.1063/5.0011358**.

68 G. Li, M. Yarali, A. Cocemasov, S. Baunack, D. L. Nika, V. M. Fomin, S. Singh, T. Gemming, F. Zhu, A. Mavrokefalos and O. G. Schmidt, In-Plane Thermal Conductivity of Radial and Planar Si/SiOx Hybrid Nanomembrane Superlattices, *ACS Nano*, 2017, **11**(8), 8215–8222, DOI: **10.1021/acsnano.7b03219**.